Article

Signatures of Polaron Dynamics in Photoexcited MAPbBr$_3$ by Infrared Spectroscopy

Published as part of The Journal of Physical Chemistry C *virtual special issue* "The Physical Chemistry of Perovskites".

Valentina Carpenella, Claudia Fasolato,* Diego Di Girolamo, Jessica Barichello, Fabio Matteocci, Caterina Petrillo, Danilo Dini, and Alessandro Nucara*

Read Online

ACCESS | Metrics & More | Article Recommendations | SI Supporting Information

ABSTRACT: Hybrid organic—inorganic perovskites (HOIPs) have attracted considerable attention in the past years as photoactive materials for low-cost, high-performance photovoltaics. Polaron formation through electron—phonon coupling has been recognized as the leading mechanism governing charge carrier transport and recombination in HOIPs. In this work, two types of MAPbBr$_3$ film samples deposited on different substrates (transparent insulating SrTiO$_3$ and a heterostructure mimicking a functioning photovoltaic cell) were photoexcited with above-bandgap radiation at 450 nm, and the effects of illumination on the sample were analyzed in the infrared region. The infrared absorbance detected at different powers of the photoexciting laser allowed us to obtain an estimate of the characteristic decay time of photoexcited polaron population of the order of 100−1000 ns. When focusing on the absorption features of the MA molecular cation in the region of the NH stretching modes, we observed the influence of hydrogen bonding and the effect of the polaron dynamics on the cation reorientation.
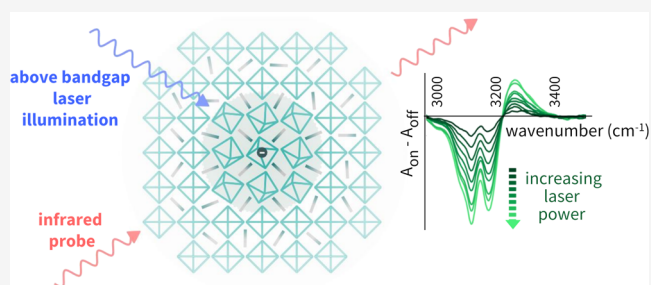
INTRODUCTION

Hybrid organic—inorganic perovskites (HOIPs) have been intensively studied in the past few decades owing to their remarkable performances in photovoltaic applications. The interest in these materials lies in their unique characteristics: direct bandgap tunable in the visible spectrum,[1] long-lived charge carriers with modest recombination rates, and long carrier diffusion lengths.[2−4] The general formula of HOIPs is ABX$_3$, in which B is a divalent metal cation (namely, Pb^{2+} or Sn^{2+}), X is a halogen anion (I$^−$, Br$^−$, or Cl$^−$) arranged in a inorganic framework of corner-sharing octahedrons, and A is a molecular cation, usually a methylammonium (of chemical formula CH$_3$NH$_3^+$ or MA) or a formamidinium (HC(NH$_2$)$_2^+$, FA), located within the voids of the inorganic lattice. The inorganic scaffold is rather soft, as already assessed by some high-pressure studies on this class of compounds,[5,6] and thus can be easily distorted through the effect of a traveling charge. It was indeed verified that, in HOIPs, the photogenerated charge carriers can couple with the polarization field of the distorted lattice, giving rise to large polarons.[7−11] The photoinduced polaron formation has been the subject of numerous studies which confirmed the Fröhlich-like nature of these quasi-particles, *i.e.*, a deformation with large spatial extension and small effective mass.[11−14] Positive (from holes)

and negative (from electrons) polarons, in fact, generate different local deformations of the lattice, which involve up to 10 unit cells, and have comparable binding energies of the order of 0.2 eV.[15] The phenomenon of self-trapping and the consequent small mobility are typical features of these quasi-particles, which have been proposed as the main factors influencing carrier recombination.[15]

In this framework, the dynamics of the monovalent cation A plays a central role, being itself affected by the local lattice distortion, while influencing the carriers' mobility, thanks to its orientational degrees of freedom.[16,17] All of the experimental data and calculation hereto available agree that the MA orientation is highly influenced by the potential energy landscape induced by the lattice deformations and by thermal energy.[18,19] In the cubic phase of these perovskites (space group *Pm*3*m*), MA can reorient almost as a freely rotating molecule on eight energetically degenerate orientations at the
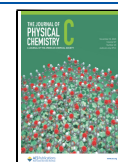
center of the cubic cell. The rate of reorientation of the cation lies in the picosecond time scale (14 ps at room temperature), and the hopping energy is well below the room-thermal activation.[18] It has been predicted that an electronic charge carrier can prompt an orientational rearrangement of the organic dipoles while crossing the crystalline lattice.[7,20] The reorientation of the MA molecule is thought to be one of the causes of charge screening, with consequent stabilization of the photogenerated carrier and prevention of fast recombination.[20]

The influence of the photoexcited polarons directly on the organic cation has been investigated so far only in a few cases. It has been commonly accepted that the cation A stabilizes and balances the spatial extent of positive and negative polarons, which, in turn, may exhibit optically active internal levels.[21−23]

The detection of photoinduced infrared-activated vibrations (IRAVs) has already been addressed as an effective way to attain evidence of polaron formation and to evaluate the importance of carrier−phonon interaction. Indeed, the IRAV peaks are observed in the absorption spectrum of a photoexcited system as a consequence of the lattice rearrangement in the excited electronic state, modifying the vibrational spectrum with relaxation of the IR selection rules, as observed in conjugated polymers and polar crystals.[24,25] An extensive investigation was provided for MAPbI$_3$.[15,21,26] Experimental evidence demonstrates that both in the ultrafast pump−probe scheme, as well as in the out-of-equilibrium spectroscopy regime obtained by continuous wave (CW) illumination, IRAV features can be regarded as direct evidence of polaron formation in the early stage of the charge relaxation process. In principle, under the same conditions, IRAV modes might provide access to the role of the molecular cations involved in polaronic excitation. It is known that the A cations, caged in the deformed lattice, may undergo both an increase in the strength of the Br−HN hydrogen bonds and a reorientation to nonenergetically degenerate configurational states, in a similar way to what is observed in the cubic-tetragonal phase transition.[19]

In this work, we investigate both the photoinduced polaron and the MA vibrational spectrum of MAPbBr$_3$. Compared to MAPbI$_3$, MAPbBr$_3$ has so far received less attention, and little is known about its energy spectrum under photoexcitation. This disparity is mainly prompted by the lower energy gap (1.4 eV) of the iodine-based HOIP, which is an appealing property for photovoltaic use. However, despite a higher gap value (∼2.3 eV), the bromide-based perovskite is less affected by moisture, oxygen, and heat under illumination;[27] hence, it is suitable for the use over longer times. Moreover, high-bandgap Br-based perovskites possess the peculiarity of being colorful and semitransparent in the visible band, therefore ideal candidates for building integrated photovoltaics in windows and façades.[28]

We focus on the mid-infrared (MIR) spectrum of MAPbBr$_3$ films deposited on different substrates. Our aim is to point out the close correlation between the steady polaron population that originated under illumination and the orientational and vibrational state of the MA molecular cations. Therefore, we first analyze in detail the spectral signatures of the large polarons formed under CW irradiation. Afterward, we focus on the vibrational spectrum of the MA cation in order to reveal the IRAV modes of the organic molecule and correlate them to the photoexcited polaron features. We observe the presence of the polaronic contribution as a broad band in the differential absorbance spectrum centered at the lowest frequencies of the

MIR spectrum. Moreover, we detected new vibrational absorptions of the MA cations in correspondence with the modes mainly involved in the hydrogen bond network. We propose that the latter may be related to the different orientational states of the MA cations within the polaron-deformed lattice regions.

■ MATERIALS AND METHODS

Sample Synthesis. The MAPbBr$_3$ films were grown on two different substrates. One of the samples (hereafter sample A) was obtained using an FTO-coated glass bulk substrate on which a heterostructure formed by NiO−Al$_2$O$_3$−PbBr$_2$ was previously deposited. NiO was deposited by spin coating of a 0.12 M NiCl$_2$ solution in 2-methoxyethanol with 10 μL/ml HNO$_3$ as a solution stabilizer. Annealing at 300 °C for 1 h results in a crystalline NiO film.[29] The mesoporous Al$_2$O$_3$ layer was deposited from a nanoparticle dispersion, starting from Sigma-Aldrich 30% weight dispersion in isopropyl alcohol (IPA) and further diluting with IPA up to 1:3. After spin coating, the film is dried at 150 °C for 10 min. Dimetilformammide (DMF) solution containing PbBr$_2$ was deposited by spin coating on top of the heterostructure. The film was subsequently heated for 10 min at 90 °C in a controlled environment and then submerged in a 15 mg/mL MABr solution in IPA, where the conversion to perovskite occurred within 5−10 min. Afterward, the perovskite film surface was rinsed with IPA and annealed at 150 °C for 10 min. The quality of the sample was tested by Raman spectroscopy (see SI Section S1 for further information). For the second sample (type B), a solution of molarity 1.4 M MABr and PbBr$_2$ dissolved in dimethyl sulfoxide (DMSO) was prepared and stirred in a nitrogen-filled glovebox for 12 h. The 0.5 mm thick SrTiO$_3$ (STO) substrate was exposed to a UV lamp for 30 min to improve the surface wettability and thus the perovskite deposition. After that, the STO substrate was heated up to 60 °C. The solution was later spun on the substrate and, after 10 s, 200 μL of ethyl acetate were dropped on the sample. Finally, the sample was sintered at 80 °C for 10 min. The thickness of the film was estimated acquiring the absorbance of the sample in three different sites of the surface on an optical benchtop setup. The three measurements, differing by less than 10%, were then averaged, and the mean thickness was calculated from the transmission value at the bandgap edge, using the conventional attenuation relation $T = T_0 \exp(-\mu \cdot d)$, where μ is the attenuation coefficient taken from the literature (∼10^5 cm^{-1}, from ref 30) and d is the sample thickness. The thickness of the perovskite film was estimated to be ∼300 nm.

The chemical degradation of the perovskite film of sample A was monitored by Raman spectroscopy. In the Raman spectra, except for an overall small decrease in the peak intensities (<20%), no new spectral features could be detected, proving that no additional chemical products have been created by environmental degradation. The physical degradation of the film, as monitored by optical microscopy, was also negligible. On sample B, only a moderate physical degradation was observed, consisting in the formation of MAPbBr$_3$ micro-crystals on the film surface, as revealed by optical microscopy. Nevertheless, the presence of crystalline microdomains on the sample did not interfere with the interpretation of our results. Both sample A and sample B were stored in the dark and in nitrogen-filled vials to avoid degradation.

Infrared Measurements. The MIR experiments on both A and B films were performed with a commercially available
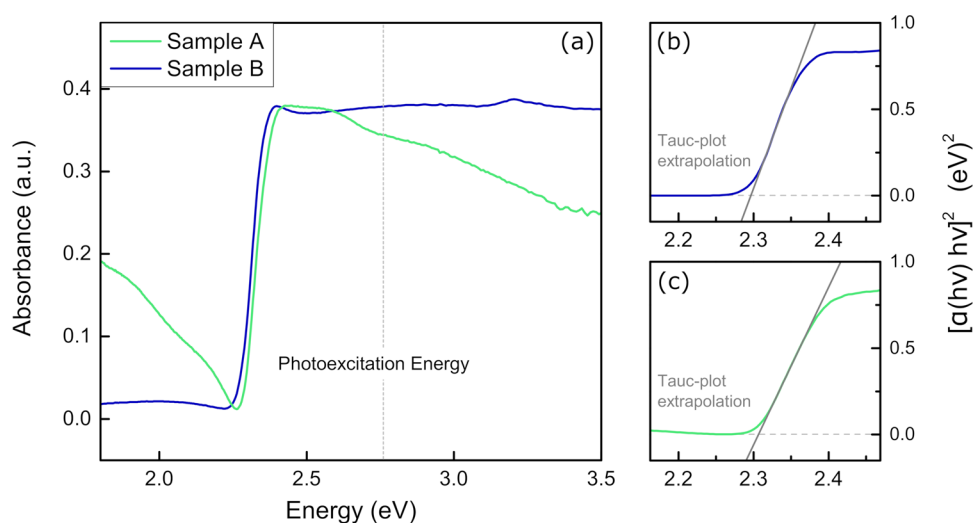
Figure 1. (a) Absorbance spectra in the UV−vis range of the MAPbBr$_3$ film of samples A (in green) and B (in blue). (b, c) Tauc plot and linear extrapolation of the energy gap of sample B and sample A, respectively.
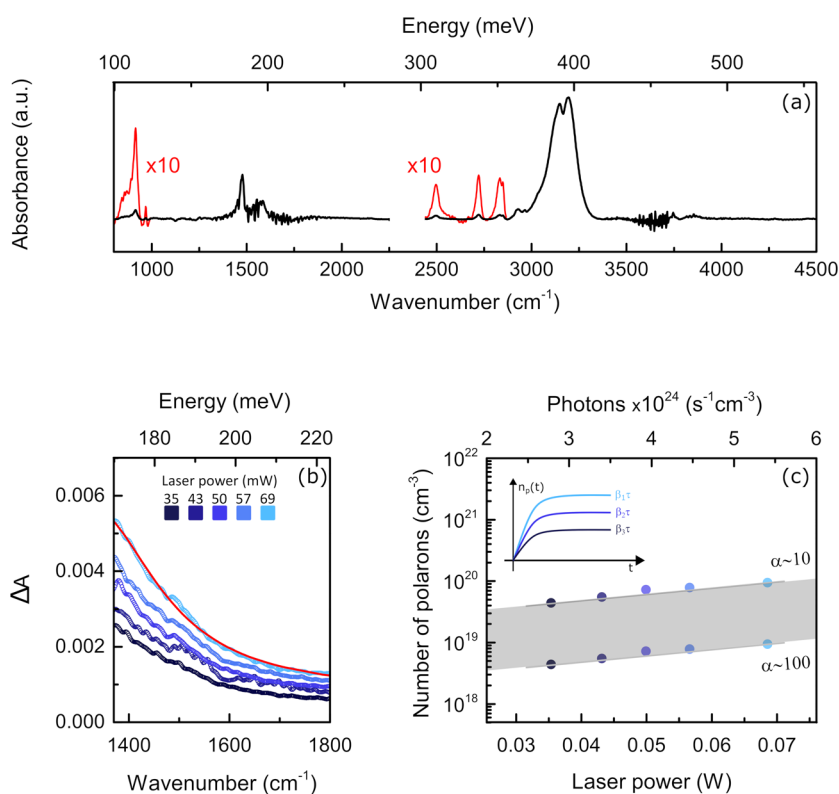
Figure 2. (a) Infrared absorbance spectrum of MAPbBr$_3$ obtained from sample A. (b) Differential absorbance (see text) of sample B below 1800 cm^{-1}. The red continuous line represents the Lorentzian fit to the polaron absorption feature. (c) Polaron density, estimated as explained in the text, as a function of laser power and incident photon density. The gray area highlights the uncertainty in the estimated polaron density values. Inset: schematic representation of polaron population over time at three different laser powers.

Bruker IFS 66v/S Fourier transform infrared (FTIR) spectrometer equipped with a Hyperion microscope working in either transmission or reflection geometry. Spectra were recorded with 2 cm^{-1} resolution coadding 64 interferograms. Sample A was measured in reflectance mode using a gold slab as a reference, as the underlying heterostructure and the glass bulk both prevent the transmission of infrared radiation. The reflectance spectra, acquired before and during photo-excitation, were collected at normal incidence through the 15× microscope objective. Samples of type B were instead measured only in transmission mode, the STO substrate being transparent above 1000 cm^{-1}, in the region of the MA vibrational modes. Algorithms from OPUS software[31] were employed for integration and atmospheric vapor and baseline correction. Both reflectance and transmittance spectra provided information on the sample absorbance $A(\omega)$ since the latter can be obtained from reflectance spectra $R(\omega)$ exploiting the usual approximation for an infinite medium, $A(\omega) \sim \log(1/R(\omega))$.

Table 1. Reports of the Polaron Lifetime from the Literature for Different HOIP Compounds

sample	polaron lifetime τ	experimental technique
MAPbI$_3$[15]	~1 ms	CW-photoexcited IR absorption spectroscopy (same as present work, but at T = 78 K)
MAPbI$_3$[38]	~140 ns	time-resolved photoluminescence and transient absorption spectroscopy
MAPbI$_3$ (polycrystalline)[39]	30 μs	steady-state photoconductivity
MAPbBr$_3$ (single crystal)[39]	~3 ms	steady-state photoconductivity
MAPbBr$_3$[40]	up to 18 μs	time-resolved photoluminescence and time-resolved infrared spectroscopy
MAPbBr$_3$[41]	100 ns	two-photon photoluminescence spectroscopy
MAPbI$_{3-x}$Cl$_x$[3]	~300 ns	ns transient absorption and time-resolved photoluminescence spectroscopy

Both A and B samples were photoexcited using a CW "pump" laser (Thorlabs PL450B laser diode, λ = 450 nm) with above-bandgap energy, focused on the film at a 45° tilt angle. The laser spot size was adjusted to match with the infrared one at the sample surface (spot size 400 × 900 μm^2). To avoid heating and damaging of the samples during illumination, many (50) spectra of short duration (~20 s) alternating on and off laser conditions were recorded and averaged. With the same approximation for an infinite medium, the differential absorbance ΔA can be evaluated directly from the ratio between the diffused reflectance collected with $(R_d^{on}(\omega))$ and without $(R_d^{off}(\omega))$ laser excitation

$$\Delta A = (A_{on} - A_{off}) = \log\left(\frac{R_d^{on}(\omega)}{R_d^{off}(\omega)}\right).$$

UV−Vis Measurements. UV−vis spectra were acquired on a Jasco V-570 spectrophotometer supplied with an ISN-470 integrating sphere attachment and a solid sample holder accessory. The UV−vis spectra of the perovskite films were obtained by comparing the diffused reflectance of the measured samples with that of a standard reference reflection plate (Spectralon).

RESULTS AND DISCUSSION

A preliminary investigation of the UV−vis absorbance of the selected HOIP films was performed to characterize our samples. The absorbance spectra of sample A (in green) and sample B (in blue) are shown in Figure 1a. The absorption edge of MAPbBr$_3$ is well evident in both samples, and minor peaks in the spectrum of sample B are observed above the gap, in agreement with those reported by Hirasawa et al.[32] The spectrum of sample A shows a general downward trend with energy (see Figure 1a) both below and above the absorption edge: this behavior is to be ascribed to the presence of the heterostructured substrate whose absorption in this range drives the total absorption observed from the whole sample (film + substrate). For more details on the substrate absorption spectrum, see SI Section 2. The analysis of the Tauc plots for both samples (Figure 1b,c) yields a bandgap value for MAPbBr$_3$ of 2.30 ± 0.01 eV, consistent with that obtained from the photoluminescence spectrum (Figure S2 in the SI) and commonly reported in the literature.[30] In this scenario, we chose to prompt above-bandgap absorption exciting the samples with laser radiation at 2.75 eV (wavelength λ= 450 nm).

Figure 2a shows the IR absorbance of the unperturbed MAPbBr$_3$ film obtained from a measurement of the reflectance of sample A. All of the infrared-active modes of the methylammonium molecule are clearly visible in the spectrum, and their energies are in good agreement with a previous study by Glaser et al.[33] The relative intensity of the bands does not match the one retrieved in transmission measurements: this is expected in the diffuse reflectivity approach since, as in this

case, wavelength dependence of the scattering from grain boundaries affects the spectral shape.[34]

The lowest frequency vibrational modes at 917 and at 968 cm^{-1} are assigned to the CH$_3$−NH$_3^+$ rocking motion and to the C−N stretching, respectively. The absorption bands at 1478 and 1582 cm^{-1} correspond to the symmetric and asymmetric NH$_3^+$ bending. At higher energies, the weak absorptions at 2497, 2721, and 2834 cm^{-1} arise from the combination of vibrational modes. Finally, the asymmetric stretching of CH$_3$ at 2963 cm^{-1} and the symmetric and asymmetric stretching of NH$_3^+$ at 3149 and 3195 cm^{-1}, respectively, are well recognized in the spectrum.

In Figure 2b, we show the absorbance variation $\Delta A = A_{on} - A_{off}$ of sample B in the region below 1800 cm^{-1}, observed in the presence of above-bandgap photoexcitation with increasing power of the external laser. In line with previous observations in MAPbI$_3$,[15,21] we ascribe these spectral changes to polaronic effects and, more precisely, to the photoionization process of a large polaron. Previous data in the literature reported polaron photoionization energies of 190 meV for MAPbI$_3$[15] and 160 meV for CsPbBr$_3$.[7] A Lorentzian fit to our data, shown in Figure 2b, provides a peak energy of 1315 cm^{-1} (163 meV), in good agreement with previous observations. For HOIPs, an intermediate electron−phonon coupling strength (α_{el-ph} ~ 1.6−1.8) is predicted in the literature;[10,35,36] thus, the polaron photoionization spectral contribution should extend somewhat above the longitudinal phonon spectral region (<200 cm^{-1}). However, for MAPbI$_3$, this band has been observed between 1200 and 1500 cm^{-1},[15,21] indicating that a stronger coupling regime occurs. Owing to the limited spectral range attainable in our measurements, we cannot confirm such an assumption, but the presence of a polaron band extending to the MIR might suggest polaron pinning in these compounds.

The intensity of ΔA shows a marked dependence on the laser power (Figure 2c). It is physically sound to assume that CW illumination generates a steady population of polarons, as illustrated in the inset of Figure 2c, whose value is $n_p = \tau\beta$, with β being the polaron photoinduction rate and τ the characteristic lifetime of the polaron population (see SI Section 3 for further details). According to ref 37, n_p can be independently estimated from the differential absorbance through the relationship $n_p \approx \Delta A/\sigma d$, where σ is the absorption cross section in the region of the polaronic absorption and d is the film thickness (d ~ 300 nm). The evaluation of the cross section σ is not straightforward, but a reasonable assessment can be derived from the average polaron volume V_p (polaronic radius 4.2 nm, according to ref 10) and the absorption coefficient α (cm^{-1}) through the relation $\sigma = V_p \cdot \alpha$. Unfortunately, α is affected by a large uncertainty, and its estimate provides values ranging from 10 to 100 cm^{-1} (see SI Section 4 for more details).

Therefore, within these approximations and making use of the values of ΔA obtained from fits to our data, we estimate a steady polaron population of the order of $10^{18}-10^{19}$ polaron/cm^3 in the illuminated region of the sample.

The top x axis in Figure 2c refers to the number of photons n delivered by the laser (see Section 5 of the SI): the rate of photoinduced polarons (β) will be proportional to the photon flux, $\beta = \varepsilon n$, where ε indicates the photon−polaron conversion efficiency. Since ε is unknown, we cannot unambiguously estimate the polaron population lifetime τ by the slope of the data in Figure 2c, but lower limits for this quantity lie in the interval between 100 and 1000 ns when assuming maximum efficiency ($\varepsilon = 1$).

Values for polaron formation time and polaron lifetime reported in the literature span several orders of magnitude, from picoseconds to milliseconds, depending on the incident energy time- and space-density, sample composition, and experimental setup. In Table 1, we report a selection of previous observations of polaron lifetime in HOIPs indicating, for each, the experimental technique employed.

In principle, a longer lifetime of the polaron population is expected when the constraints of the bottleneck effect are fulfilled.[42−44] Indeed, the lowest decay times seem to be observed at the smallest carrier densities and in pump−probe experiments: the time scales of pump−probe optical approaches are much faster than the lattice relaxation dynamics, meaning that the incident photons probe the polarons over time scales shorter than their thermalization with the lattice, which is thus still "cold" at such short delays. Conversely, in CW experiments, the local heating of the sample and the slow detection procedures give access to the polaron−thermal bath interaction. Indeed, upon CW illumination, LA phonon states are also excited (we remark that a local temperature around 400 K was estimated in our experiment, as reported in Section 6 of the SI), so that the exceeding LA steady population enhances the phonon bottleneck effect, providing even longer decay times for polarons. It is worth noting that high concentrations of photocarriers ($>10^{18}$) are also predicted to inhibit polaron stabilization in pump−probe regimes;[45,46] however, an effective threshold is not available in the literature nor this effect has been predicted to exist in CW experiments, where the interaction of polarons with a warm lattice bath plays the key role.

The differential absorption ΔA, measured on sample A in the MIR region, is shown in Figure 3. At the main vibrational modes (see Figure 2a), the ΔA spectra exhibit both positive (gray areas in Figure 3) and negative (light-blue areas) features. The negative values of ΔA are in correspondence to the absorption peaks measured on the unperturbed sample, meaning that absorption is suppressed by the photoexcitation. These marked drops in the differential spectrum are accompanied by positive ΔA features at higher wavenumbers, which imply the appearance of new IR-active absorptions in the photoexcited film, close to the unperturbed vibrational modes. Such ΔA variations occur in each vibrational mode of MA but are much more evident for the intense NH stretching above 2900 cm^{-1}. We remark that direct thermal effects for these vibrational energies can be definitely excluded, as thoroughly discussed in Section S6 of the SI.

As shown in Figure 3, fitting the negative region of the spectrum returns two modes centered at 3138 and 3195 cm^{-1}, in correspondence, within the experimental error, to the NH$_3^+$
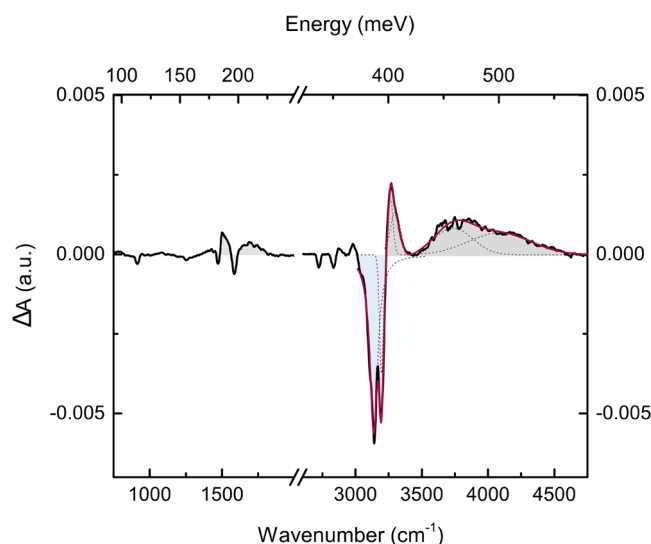

Figure 3. Variation of the absorbance spectrum of sample A observed upon continuous illumination with 450 nm, 69 mW laser photo-excitation. The quantity ΔA is defined as $\Delta A = A_{on} - A_{off}$ (see the text). Positive and negative contributions to the spectrum are highlighted, respectively, in gray and light blue. The Gaussian fitting deconvolution of the positive and negative contributions is indicated by the dashed lines.

symmetric and asymmetric stretching, respectively; the two broad bands at positive ΔA are observed at higher wavenumbers, the first centered at 3281 cm^{-1}, about 100 cm^{-1} from the central frequency of the unperturbed band, and the other, broader and less intense, with maximum at 3750 cm^{-1}, shifted from the same band by $\sim$600 cm^{-1}.

In the case of the MAPbBr$_3$ film deposited on a bare SrTiO$_3$ (sample B), the transmission measurements in the same NH stretching region highlighted only the most intense positive band (Figure S4 of the SI) due to the unfavorable signal/noise ratio of the setup; however, the features found in transmission experiments provide a further validation of the reflectivity experiments. We note that the differential absorbance from sample A (Figure 4a) is at least an order of magnitude higher than that of sample B (Figure S5 of SI, Section 7). However, we remark that experimental configurations adopted to measure samples A and B are quite different (diffuse reflectance for the former and direct transmission for the latter) so that physical parameters, such as sample thickness and diffusion efficiency, prevent a reliable quantitative comparison between the samples. Therefore, we can only infer qualitatively that MA vibrational changes occur in both samples.

An explicative magnification on the regions of interest at different laser power excitations is shown in Figure 4a,b. The area of the negative ΔA region and the sum of the two positive areas obtained from Sample A are shown as a function of pump power in Figure 4c. The enhancement of the negative area versus power reveals the progressive depopulation of the vibrational NH$_3^+$ ground states. It is indeed remarkable that the sum of the positive areas follows the same linear trend as that of the negative one, suggesting that the fraction of NH oscillators leaving the unperturbed vibrational ground state (negative area) strictly matches the increase in the population of new vibrational ground states (positive area).
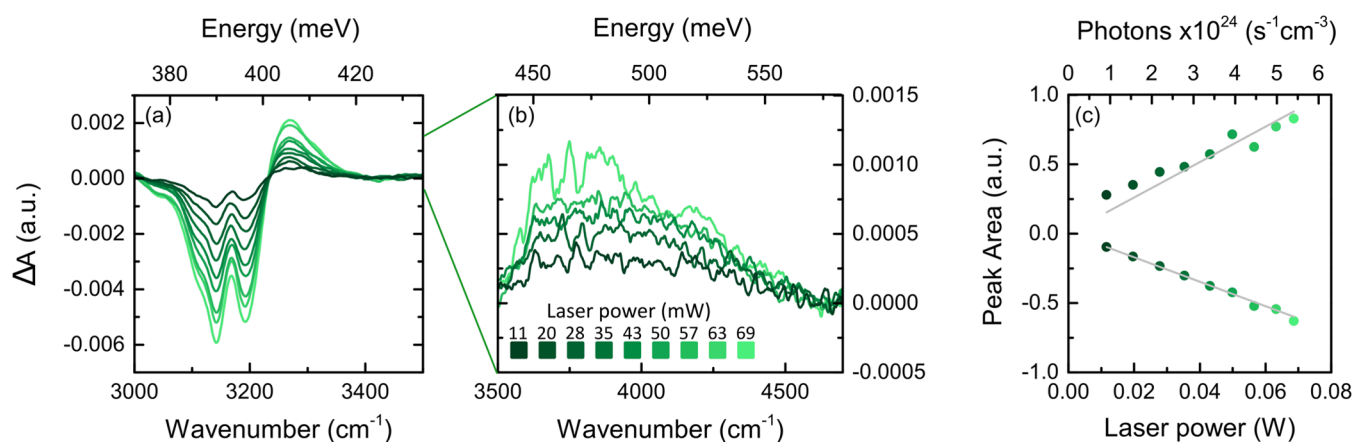
Figure 4. (a, b) Differential absorbance spectra of sample A at different output powers of the pumping laser beam in the range of 3000−3500 and 3500−4700 cm^{-1}, respectively. Some data in panel (b) are omitted for the sake of clarity. The baseline subtraction performed on these spectra is discussed in Section S8 of the SI. (c) Calculated peak areas in the range of 3000−4500 cm^{-1} as a function of laser power and the number of photons impinging on the sample.

The emergence of new vibrational modes in polar crystals is a well-established occurrence.[24,25,47] It is well-known that IRAV modes originate from polarons since they arise in polar lattices as a result of the local deformations induced around charges and are indicative of the coupling between the charged excitation and the surrounding lattice.[25] However, IRAVs signatures are expected primarily at low wavenumbers (below 500 cm^{-1}), i.e., close to the absorption lines of the main phonons. The spectral features here observed in ΔA are IRAV modes ascribable to a different effect: our hypothesis is that the motion of the organic cation is heavily affected by the polaronic lattice deformation through the elongation and/or the shortening of the Br−H hydrogen bonds. We hypothesize that the steady polaron population formed upon irradiation distorts the inorganic lattice involving a significant percentage of the organic molecular cations (estimated at around 10% of the total MA cations). These lattice distortions could temporarily "freeze" the MA cations in specific orientations where they experience different hydrogen bond strengths with the surrounding Br$^-$ ions. Indeed, as already discussed by Stallhofer et al. for MAPbI$_3$,[21] changes in the bond strength between atoms can result in a frequency shift of the IR modes. Recently, Lee and co-workers[19] asserted that the 8-fold degenerate orientational states of the MA ion in the cubic O_h symmetry are grouped into two manifolds of states when lattice changes into the tetragonal D_{2d} symmetry; this degeneracy breaking is a consequence of H bonding strength changes. In this scenario, the two positive bands observed in our ΔA spectra above 3200 cm^{-1} could be considered as the vibrational bands of MA ions frozen in two main orientational configurations within lattice regions distorted by the presence of polarons. As mentioned in ref 19, the energy gap between the two locked orientations in the D_{2d} symmetry phase (see Section S9 of the SI) is theoretically estimated at around 90 meV, thus in good agreement with the energy difference ΔE that we obtain from the peak energies of the observed bands. We cannot push the analogy with the ordered orientational phase D_{2d} any further, as the photoinduced distortion could produce local strains with different ion arrangements. A more detailed analysis of the photogenerated IRAV modes shows that each one of them is composed of two bands, and a qualitative deconvolution with Gaussian lines is shown in Figure 3. The presence of multiple contributions for each band

can be related either to a slightly different lattice deformations due to positive (holes) and negative (electrons) polarons or to a further symmetry removal between the manifold of orientational states. The binding energy difference between positive and negative polarons in MAPbI$_3$ is of the order of 0.05 eV,[15] a value similar to the difference of the central energy of the two Gaussian components describing the IRAV vibrational mode at 3750 cm^{-1}. As for the deconvolution of the IRAV feature at lower frequency (centered around 3250 cm^{-1}), the Gaussian lines are separated only by 40 cm^{-1} (0.005 eV); therefore, a degeneration removal between orientational states appears as a more plausible hypothesis for such a fine structure.

■ CONCLUSIONS

In this work, we studied the MIR spectrum of two samples of MAPbBr$_3$: a heterostructure whose composition mimics a working photovoltaic cell and a perovskite film on SrTiO$_3$ which, in the context of this work, was used to confirm the main results and to better highlight the spectral contributions in the polaronic regions. For the first time, to our knowledge, the contribution of polarons in the MIR as a function of the optical output power of the pump laser in MAPbBr$_3$ was explored, thus linking the IRAV spectral modifications associated with the MA vibrational features to the estimated photoexcited polaron population. The experimental data confirm the long lifetime, 100−1000 ns, of this population of quasi-particles. Their excitation energies are found to be higher than those expected from the Fröhlich models of large polarons: the combination of the two outcomes suggests a picture of soft large polarons trapped in the lattice, similar to those observed in iodine-based HOIPs. The above-gap irradiation also affects the vibrational states of the molecular organic ions, with the rise of new absorption bands to the detriment of the population of the fundamental levels of the unperturbed states. Our hypothesis is that these IRAVs are related to modified orientational configurations of the methylammonium ions, following the deformation of the lattice produced by the polarons.

This work provides a solid experimental approach to the study of the orientational and vibrational dynamics of the organic cations of HOIPs and highlights the close correlation

between the local lattice strains and the degrees of freedom of the organic molecules. The knowledge of the relevant coupling mechanisms between organic−inorganic lattices can provide indications of polaron photoexcitation in HOIPs that are not yet fully understood. The results presented here are relevant for the engineering of materials suitable for use in photovoltaics: indeed, the present approach could highlight the role of the organic cations in determining the lifetime and mobility of the excited charge states and suggest routes to tailor these properties.

■ ASSOCIATED CONTENT

Ⓢ Supporting Information

The Supporting Information is available free of charge at https://pubs.acs.org/doi/10.1021/acs.jpcc.3c03668.

> Further details on the sample characterization and on the analysis of the differential absorbance spectra (PDF)

■ AUTHOR INFORMATION

Corresponding Authors

Claudia Fasolato − *CNR-ISC, Istituto dei Sistemi Complessi, 00185 Rome, Italy;* ⓞ orcid.org/0000-0003-3450-404X; Email: claudia.fasolato@cnr.it

Alessandro Nucara − *CNR-SPIN and Department of Physics, Sapienza University of Rome, 00185 Rome, Italy;* Email: alessandro.nucara@uniroma1.it

Authors

Valentina Carpenella − *Department of Sciences, University of Roma Tre, 00146 Rome, Italy;* ⓞ orcid.org/0000-0002-0631-8189

Diego Di Girolamo − *Department of Chemistry, Sapienza University of Rome, 00185 Rome, Italy*

Jessica Barichello − *CHOSE, Department of Electronic Engineering, University of Rome Tor Vergata, Rome 00133, Italy;* ⓞ orcid.org/0000-0003-1277-4217

Fabio Matteocci − *CHOSE, Department of Electronic Engineering, University of Rome Tor Vergata, Rome 00133, Italy*

Caterina Petrillo − *Department of Physics and Geology, University of Perugia, 06123 Perugia, Italy*

Danilo Dini − *Department of Chemistry, Sapienza University of Rome, 00185 Rome, Italy;* ⓞ orcid.org/0000-0001-5005-4187

Complete contact information is available at:
https://pubs.acs.org/10.1021/acs.jpcc.3c03668

Author Contributions

V.C. and A.N performed the measurements and the data analysis and wrote the main draft. D.D.G. synthesized the MAPbBr$_3$ heterostructure. J.B. and F.M. synthesized the MAPbBr$_3$ film on SrTiO$_3$. C.F., D.D., and C.P. contributed to the interpretation of the results and critically reviewed the paper. A.N. conceived the work and supervised it together with C.F. All authors discussed the results and revised the article. All authors have given approval to the final version of the manuscript.

Notes

The authors declare no competing financial interest.

■ REFERENCES

(1) Zuo, T.; He, X.; Hu, P.; Jiang, H. Organic-Inorganic Hybrid Perovskite Single Crystals: Crystallization, Molecular Structures, and Bandgap Engineering. *ChemNanoMat* **2019**, *5* (3), 278−289.

(2) Wehrenfennig, C.; Eperon, G. E.; Johnston, M. B.; Snaith, H. J.; Herz, L. M. High charge carrier mobilities and lifetimes in organolead trihalide perovskites. *Adv. Mater.* **2014**, *26* (10), 1584−1589.

(3) Stranks, S. D.; Eperon, G. E.; Grancini, G.; Menelaou, C.; Alcocer, M. J.; Leijtens, T.; Herz, L. M.; Petrozza, A.; Snaith, H. J. Electron-hole diffusion lengths exceeding 1 micrometer in an organometal trihalide perovskite absorber. *Science* **2013**, *342* (6156), 341−344.

(4) Xing, G.; Mathews, N.; Sun, S.; Lim, S. S.; Lam, Y. M.; Grätzel, M.; Mhaisalkar, S.; Sum, T. C. Long-range balanced electron-and hole-transport lengths in organic-inorganic CH$_3$NH$_3$PbI$_3$. *Science* **2013**, *342* (6156), 344−347.

(5) Capitani, F.; Marini, C.; Caramazza, S.; Dore, P.; Pisanu, A.; Malavasi, L.; Nataf, L.; Baudelet, F.; Brubach, J.-B.; Roy, P.; et al. Locking of methylammonium by pressure-enhanced H-bonding in (CH$_3$NH$_3$)PbBr$_3$ hybrid perovskite. *J. Phys. Chem. C* **2017**, *121* (50), 28125−28131.

(6) Carpenella, V.; Ripanti, F.; Stellino, E.; Fasolato, C.; Nucara, A.; Petrillo, C.; Malavasi, L.; Postorino, P. High-Pressure Behavior of δ-Phase of Formamidinium Lead Iodide by Optical Spectroscopies. *J. Phys. Chem. C* **2023**, *127* (5), 2440−2447.

(7) Meggiolaro, D.; Ambrosio, F.; Mosconi, E.; Mahata, A.; De Angelis, F. Polarons in metal halide perovskites. *Adv. Energy Mater.* **2020**, *10* (13), No. 1902748.

(8) Zheng, F.; Wang, L. W. Large polaron formation and its effect on electron transport in hybrid perovskites. *Energy Environ. Sci.* **2019**, *12* (4), 1219−1230.

(9) Zhu, X. Y.; Podzorov, V. Charge carriers in hybrid organic−inorganic lead halide perovskites might be protected as large polarons. *J. Phys. Chem. Lett.* **2015**, *6* (23), 4758−4761.

(10) Miyata, K.; Meggiolaro, D.; Trinh, M. T.; Joshi, P. P.; Mosconi, E.; Jones, S. C.; De Angelis, F.; Zhu, X. Y. Large polarons in lead halide perovskites. *Sci. Adv.* **2017**, *3* (8), No. e1701217.

(11) Jin, Z.; Peng, Y.; Fang, Y.; Ye, Z.; Fan, Z.; Liu, Z.; Bao, X.; Gao, H.; Ren, W.; Wu, J.; et al. Photoinduced large polaron transport and dynamics in organic−inorganic hybrid lead halide perovskite with terahertz probes. *Light: Sci. Appl.* **2022**, *11* (1), No. 209.

(12) Bonn, M.; Miyata, K.; Hendry, E.; Zhu, X. Y. Role of dielectric drag in polaron mobility in lead halide perovskites. *ACS Energy Lett.* **2017**, *2* (11), 2555−2562.

(13) Miyata, A.; Mitioglu, A.; Plochocka, P.; Portugall, O.; Wang, J. T. W.; Stranks, S. D.; Snaith, H. J.; Nicholas, R. J. Direct measurement of the exciton binding energy and effective masses for charge carriers in organic−inorganic tri-halide perovskites. *Nat. Phys.* **2015**, *11* (7), 582−587.

(14) Cinquanta, E.; Meggiolaro, D.; Motti, S. G.; Gandini, M.; Alcocer, M. J.; Akkerman, Q. A.; Vozzi, C.; Manna, L.; De Angelis, F.; Petrozza, A.; et al. Ultrafast THz probe of photoinduced polarons in lead-halide perovskites. *Phys. Rev. Lett.* **2019**, *122* (16), No. 166601.

(15) Wong, W. P.; Yin, J.; Chaudhary, B.; Chin, X. Y.; Cortecchia, D.; Lo, S. Z. A.; Grimsdale, A. C.; Mohammed, O. F.; Lanzani, G.; Soci, C. Large polaron self-trapped states in three-dimensional metal-halide perovskites. *ACS Mater. Lett.* **2020**, *2* (1), 20−27.

(16) Neukirch, A. J.; Nie, W.; Blancon, J. C.; Appavoo, K.; Tsai, H.; Sfeir, M. Y.; Katan, C.; Pedesseau, L.; Even, J.; Crochet, J. J.; et al. Polaron stabilization by cooperative lattice distortion and cation rotations in hybrid perovskite materials. *Nano Lett.* **2016**, *16* (6), 3809−3816.

(17) Mehdizadeh, A.; Akhtarianfar, S. F.; Shojaei, S. Role of methylammonium rotation in hybrid halide MAPbX$_3$ (X= I, Br, and Cl) perovskites by a density functional theory approach: Optical and electronic properties. *J. Phys. Chem. C* **2019**, *123* (11), 6725−6734.

(18) Leguy, A. M.; Frost, J. M.; McMahon, A. P.; Sakai, V. G.; Kockelmann, W.; Law, C.; Li, X.; Foglia, F.; Walsh, A.; O'regan, B. C.; et al. The dynamics of methylammonium ions in hybrid organic−inorganic perovskite solar cells. *Nat. Commun.* **2015**, *6* (1), No. 7124.

(19) Lee, J. H.; Lee, J. H.; Kong, E. H.; Jang, H. M. The nature of hydrogen-bonding interaction in the prototypic hybrid halide perovskite, tetragonal CH$_3$NH$_3$PbI$_3$. *Sci. Rep.* **2016**, *6* (1), No. 21687.

(20) Zhu, H.; Miyata, K.; Fu, Y.; Wang, J.; Joshi, P. P.; Niesner, D.; Williams, K. W.; Jin, S.; Zhu, X. Y. Screening in crystalline liquids protects energetic carriers in hybrid perovskites. *Science* **2016**, *353* (6306), 1409−1413.

(21) Stallhofer, K.; Nuber, M.; Cortecchia, D.; Bruno, A.; Kienberger, R.; Deschler, F.; Soci, C.; Iglev, H. Picosecond Charge Localization Dynamics in CH$_3$NH$_3$PbI$_3$ Perovskite Probed by Infrared-Activated Vibrations. *J. Phys. Chem. Lett.* **2021**, *12* (18), 4428−4433.

(22) Munson, K. T.; Swartzfager, J. R.; Gan, J.; Asbury, J. B. Does dipolar motion of organic cations affect polaron dynamics and bimolecular recombination in halide perovskites? *J. Phys. Chem. Lett.* **2020**, *11* (8), 3166−3172.

(23) Munson, K. T.; Doucette, G. S.; Kennehan, E. R.; Swartzfager, J. R.; Asbury, J. B. Vibrational probe of the structural origins of slow recombination in halide perovskites. *J. Phys. Chem. C* **2019**, *123* (12), 7061−7073.

(24) Miranda, P. B.; Moses, D.; Heeger, A. J. Ultrafast photo-generation of charged polarons in conjugated polymers. *Phys. Rev. B* **2001**, *64* (8), No. 081201.

(25) Kim, Y. H.; Heeger, A. J.; Acedo, L.; Stucky, G.; Wudl, F. Direct evidence of the importance of electron-phonon coupling in La$_2$CuO$_4$: Photoinduced ir-active vibrational modes. *Phys. Rev. B* **1987**, *36* (13), 7252.

(26) Ivanovska, T.; Dionigi, C.; Mosconi, E.; De Angelis, F.; Liscio, F.; Morandi, V.; Ruani, G. Long-lived photoinduced polarons in organohalide perovskites. *J. Phys. Chem. Lett.* **2017**, *8* (13), 3081−3086.

(27) Sun, Q.; Liu, X.; Cao, J.; Stantchev, R. I.; Zhou, Y.; Chen, X.; Parrott, E. P. J.; Lloyd-Hughes, J.; Zhao, N.; Pickwell-MacPherson, E. Highly sensitive terahertz thin-film total internal reflection spectroscopy reveals in situ photoinduced structural changes in methyl-ammonium lead halide perovskites. *J. Phys. Chem. C* **2018**, *122* (30), 17552−17558.

(28) Barichello, J.; Di Girolamo, D.; Nonni, E.; Paci, B.; Generosi, A.; Kim, M.; Levtchenko, A.; Cacovich, S.; Di Carlo, A.; Matteocci, F. Semi-Transparent Blade-Coated FAPbBr3 Perovskite Solar Cells: A Scalable Low-Temperature Manufacturing Process under Ambient Condition. *Solar RRL* **2023**, *7* (3), No. 2200739.

(29) Di Girolamo, D.; Phung, N.; Jošt, M.; Al-Ashouri, A.; Chistiakova, G.; Li, J.; Marquez, J. A.; Unold, T.; Korte, L.; Albrecht, S.; et al. From bulk to surface: sodium treatment reduces recombination at the nickel oxide/perovskite interface. *Adv. Mater. Interfaces* **2019**, *6* (17), No. 1900789.

(30) Mannino, G.; Deretzis, I.; Smecca, E.; La Magna, A.; Alberti, A.; Ceratti, D.; Cahen, D. Temperature-dependent optical band gap in CsPbBr$_3$, MAPbBr$_3$, and FAPbBr$_3$ single crystals. *J. Phys. Chem. Lett.* **2020**, *11* (7), 2490−2496.

(31) https://www.bruker.com/en/products-and-solutions/infrared-and-raman/opus-spectroscopy-software.html.

(32) Hirasawa, M.; Ishihara, T.; Goto, T. Exciton features in 0-, 2-, and 3-dimensional networks of [PbI$_6$]$^{4+}$ octahedra. *J. Phys. Soc. Jpn.* **1994**, *63* (10), 3870−3879, DOI: 10.1143/JPSJ.63.3870.

(33) Glaser, T.; Müller, C.; Sendner, M.; Krekeler, C.; Semonin, O. E.; Hull, T. D.; Yaffe, O.; Owen, J. S.; Kowalsky, W.; Pucci, A.; et al. Infrared spectroscopic study of vibrational modes in methylammonium lead halide perovskites. *J. Phys. Chem. Lett.* **2015**, *6* (15), 2913−2918.

(34) Spragg, R.; Seer Green, U. K.. Reflection measurements in IR spectroscopy *Perkin Elmer: Technical Note* 2013.

(35) Chan, C. C.; Fan, K.; Wang, H.; Huang, Z.; Novko, D.; Yan, K.; Xu, J.; Choy, W. C. H.; Lončarić, I.; Wong, K. S. Uncovering the electron-phonon interplay and dynamical energy-dissipation mecha-nisms of hot carriers in hybrid lead halide perovskites. *Adv. Energy Mater.* **2021**, *11* (9), No. 2003071.

(36) Puppin, M.; Polishchuk, S.; Colonna, N.; Crepaldi, A.; Dirin, D. N.; Nazarenko, O.; De Gennaro, R.; Gatti, G.; Roth, S.; Barillot, T.; et al. Evidence of large polarons in photoemission band mapping of the perovskite semiconductor CsPbBr$_3$. *Phys. Rev. Lett.* **2020**, *124* (20), No. 206402.

(37) List, E. J. W.; Kim, C. H.; Naik, A. K.; Scherf, U.; Leising, G.; Graupner, W.; Shinar, J. Interaction of singlet excitons with polarons in wide band-gap organic semiconductors: A quantitative study. *Phys. Rev. B* **2001**, *64* (15), No. 155204.

(38) Yamada, Y.; Nakamura, T.; Endo, M.; Wakamiya, A.; Kanemitsu, Y. Photocarrier recombination dynamics in perovskite CH$_3$NH$_3$PbI$_3$ for solar cell applications. *J. Am. Chem. Soc.* **2014**, *136* (33), 11610−11613, DOI: 10.1021/ja506624n.

(39) Chen, Y.; Yi, H. T.; Wu, X.; Haroldson, R.; Gartstein, Y. N.; Rodionov, Y. I.; Tikhonov, K. S.; Zakhidov, A.; Zhu, X. Y.; Podzorov, V. Extended carrier lifetimes and diffusion in hybrid perovskites revealed by Hall effect and photoconductivity measurements. *Nat. Commun.* **2016**, *7* (1), No. 12253.

(40) Miyata, K.; Nagaoka, R.; Hada, M.; Tanaka, T.; Mishima, R.; Kuroda, T.; Sueta, S.; Iida, T.; Yamashita, Y.; Nishikawa, T.; et al. Liquid-like dielectric response is an origin of long polaron lifetime exceeding 10 μs in lead bromide perovskites. *J. Chem. Phys.* **2020**, *152* (8), No. 084704, DOI: 10.1063/1.5127993.

(41) Karki, K. J.; Abdellah, M.; Zhang, W.; Pullerits, T. Different emissive states in the bulk and at the surface of methylammonium lead bromide perovskite revealed by two-photon micro-spectroscopy and lifetime measurements. *APL Photonics* **2016**, *1* (4), No. 046103, DOI: 10.1063/1.4948645.

(42) Miyata, K.; Atallah, T. L.; Zhu, X. Y. Lead halide perovskites: Crystal-liquid duality, phonon glass electron crystals, and large polaron formation. *Sci. Adv.* **2017**, *3* (10), No. e1701469.

(43) Yang, J.; Wen, X.; Xia, H.; Sheng, R.; Ma, Q.; Kim, J.; Tapping, P.; Harada, T.; Kee, T. W.; Huang, F.; et al. Acoustic-optical phonon up-conversion and hot-phonon bottleneck in lead-halide perovskites. *Nat. Commun.* **2017**, *8* (1), No. 14120.

(44) Yang, Y.; Ostrowski, D. P.; France, R. M.; Zhu, K.; Van De Lagemaat, J.; Luther, J. M.; Beard, M. C. Observation of a hot-phonon bottleneck in lead-iodide perovskites. *Nat. Photonics* **2016**, *10* (1), 53−59.

(45) Niesner, D.; Zhu, H.; Miyata, K.; Joshi, P. P.; Evans, T. J.; Kudisch, B. J.; Trinh, M. T.; Marks, M.; Zhu, X. Y. Persistent energetic electrons in methylammonium lead iodide perovskite thin films. *J. Am. Chem. Soc.* **2016**, *138* (48), 15717−15726.

(46) Emin, D. *Polarons*; Cambridge University Press, 2013.

(47) Federici, J. F.; Greene, B. I.; Rapkine, D. H.; Orenstein, J. Thermally activated infrared-active vibrational mode in BaBiO$_3$. *Phys. Rev. B* **1991**, *43* (10), 8617.